Robust Far-Field Optical Image Transmission with Structured Random Light Beams

Yonglei Liu,[1] Xuan Zhang,[2] Zhen Dong,[2] Deming Peng,[2] Yahong Chen,[2,*] Fei Wang,[2,†] and Yangjian Cai[1,2,‡]

[1] *Shandong Provincial Engineering and Technical Center of Light Manipulation and Shandong Provincial Key Laboratory of Optics and Photonic Devices, School of Physics and Electronics, Shandong Normal University, Jinan 250014, China*

[2] *Institute of Optics, School of Physical Science and Technology, Soochow University, Suzhou 215006, China*

(Received 11 October 2021; revised 7 December 2021; accepted 5 January 2022; published 15 February 2022)

The ability to overcome the adverse effect induced by the obstacles within the transmission link is a central challenge in long-distance optical image transmission and is significantly crucial in free-space optical communication. In this work, we introduce an efficient protocol to realize the robust far-field optical image-signal transmission by modulating the spatial-coherence structure of a partially coherent random light source. The image information encoded in the spatial-coherence structure can be stably transmitted to the far field and can resist the influence of obstructions within the communication link. This is due to the self-reconstruction property of the spatial-coherence structure embedded with the cross phase in the far field. We demonstrate experimentally that the image information can be recovered well by measuring the second-order spatial-coherence structure of the obstructed random light in the far field. Our findings open a door for robust optical signal transmission through the complex environment and may find application in optical communication through a turbulent atmosphere.

DOI: 10.1103/PhysRevApplied.17.024043

I. INTRODUCTION

Long-distance optical image-signal transmission is fundamentally significant in the application of free-space optical communication [1,2]. However, the obstacles, such as the aerosol, a turbulent atmosphere, within the communication channel limit the performance of information transmission and cause distortion, scintillation, and random spatial shifts of the output image [3,4]. The self-healing property of structured light beams, including Airy beams [5–7], helical beams [8,9], and vector beams with complex polarization states [10–12], can (partially) resist the side effects induced by the obstructions or the turbulent atmosphere in the transmission path. The structured beams used so far have been restricted to fully coherent circumstances. Thus, the speckle noise in the output image cannot be neglected [13]. Moreover, when the size of the obstacles is large enough or the strength of the turbulent atmosphere is strong within the propagation link, the non-negligible interference effects will distort the quality of the image signal [4].

In this work, we introduce a different way to robustly transmit optical images to the far field with the use of partially coherent random light beams that have customized spatial-coherence structures. It has been well recognized that a partially coherent light beam has advantages in free-space optical communication [14–21], speckle-free imaging [22,23], and high-quality diffractive imaging [24,25] due to its low spatial-coherence property [26,27]. Recently, it has been found that partially coherent beams have a self-reconstruction feature similar to that of fully coherent diffraction-free beams during propagation in free space [28–30]. However, their physical interpretations are quite different. The reconstruction capacity of a partially coherent beam is closely related to its small spatial-coherence area [28]. On the other hand, it has been shown that the spatial-coherence structure of the partially coherent beam can be viewed as an efficient degree of freedom to govern its propagation properties [31–33]. Partially coherent beams with tailored spatial-coherence structures have been found useful in spatial information transmission in the near field [34,35] and in the robust $4f$ imaging system [36,37]. More recently, the spatial-coherence structure has been used to encrypt optical image information in a random source and has been shown to be robust during measurement in different complex media [38,39].

However, long-distance and far-field image-signal transmission based on modulation of the spatial-coherence

---

[*] yahongchen@suda.edu.cn

[†] fwang@suda.edu.cn

[‡] yangjiancai@suda.edu.cn

structure of a partially coherent light beam is still challenging because the spatial-coherence structure changes during propagation in free space and turbulent atmospheres [26]. In the far field, the spatial-coherence structure for a lowly spatially coherent beam is mainly determined by the initial intensity of the source [27,40]. Thus, the image information encoded ahead in the spatial-coherence structure of the partially coherent source cannot be recovered through the far-field coherence measurement. In this work, we find that by introducing a second-order cross phase [41–43] into the spatial-coherence structure of the partially coherent source, the far-field spatial-coherence distribution can be reconstructed well even with large obstacles in the propagation channel. Thus, the image information encoded in the spatial-coherence structure can be robustly transmitted to the far field. We demonstrate theoretically and experimentally that the encoded image can be recovered well in the far field solely by measuring the far-zone modulus distribution of the spatial-coherence structure of the obstructed random light. The effect of the spatial-coherence area on the recovered image quality is analyzed in detail as well. Our coherence-based approach to far-field image-signal transmission may open an avenue for optical imaging and communications in a complex environment.

This work is organized as follows. In Sec. II, we present the basic principle and the theoretical background of coherence-based far-field image transmission. In Sec. III, we show the simulation results for the intensity and the spatial degree of coherence as well as the recovered image signal in the focal plane. The effect of the initial spatial-coherence area on image quality is also discussed in this section. In Sec. IV, we carry out a proof-of-principle experiment to show the robustness of our coherence-based image-signal transmission method. Finally, in Sec. V we summarize our findings.

II. PRINCIPLE

In this section, we unveil the principle and the theoretical background of coherence-based optical image transmission. The schematic, including the image encoding into a partially coherent random source, the propagation of a partially coherent beam in a transmission link with obstacles, and the far-field image recovery, is shown in Fig. 1.

A. Encoding image into spatial-coherence structure

The second-order statistical property of a partially coherent light beam is characterized by a (two-point) spatial-coherence function [26]. In the spatial-frequency domain, the spatial-coherence function is described by the cross-spectral density function as $W_s(\mathbf{r}_1, \mathbf{r}_2, \omega) = \langle E^*(\mathbf{r}_1, \omega) E(\mathbf{r}_2, \omega)\rangle$, where the subscript s denotes the source, $\mathbf{r}_1$ and $\mathbf{r}_2$ are two arbitrary spatial points in the source plane, $E(\mathbf{r}, \omega)$ is a random-field realization, and the asterisk and the angle brackets denote the complex conjugate and the ensemble average over all field realizations, respectively. The angular frequency ω is omitted from now on to simplify the notation.

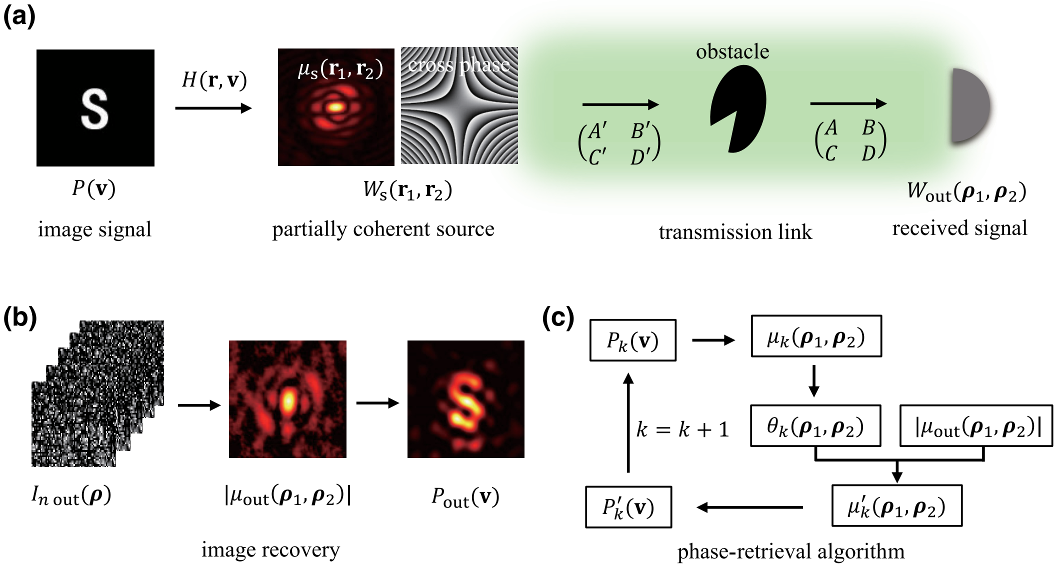

FIG. 1. A schematic of the principle for far-field optical image transmission with a structured random light beam. (a) The image signal with transmission function $P(\mathbf{v})$ is encoded into the second-order cross-spectral density $W_s(\mathbf{r}_1, \mathbf{r}_2)$ of a partially coherent light source via the optical system with the response function $H(\mathbf{r}, \mathbf{v})$. The partially coherent beam propagates in a transmission link within a sector-shaped obstacle. (b) The modulus of the spatial degree of coherence, $|\mu_{out}(\boldsymbol{\rho}_1, \boldsymbol{\rho}_2)|$, in the output plane can be obtained from the received intensity speckles $I_{n\,out}(\boldsymbol{\rho})$. The image signal $P_{out}(\mathbf{v})$ can be recovered by using the phase-retrieval algorithm shown in (c).

To see the inner structure of a spatial-coherence function, the cross-spectral density can also be written in the following integral form [44,45]:

$$W_s(\mathbf{r}_1,\mathbf{r}_2)=\iint P(\mathbf{v})H^*(\mathbf{r}_1,\mathbf{v})H(\mathbf{r}_2,\mathbf{v})d^2\mathbf{v}, \quad (1)$$

where $P(\mathbf{v})$ is a non-negative function and $H(\mathbf{r},\mathbf{v})$ is an arbitrary kernel function that connects the $P(\mathbf{v})$ at the $\mathbf{v}$ domain and $W_s(\mathbf{r}_1,\mathbf{r}_2)$ at the $\mathbf{r}$ domain. The above integral form is useful for synthesis of partially coherent sources with a controllable spatial-coherence structure if we consider the $P(\mathbf{v})$ function as the intensity distribution of an incoherent source and the $H(\mathbf{r},\mathbf{v})$ function as a response function of the optical system between the incoherent source and the generated partially coherent source [46–48].

Here, we regard $P(\mathbf{v})$ as the transmission function of an optical image. It can be transformed into the intensity of the incoherent source by passing the fully coherent light through a rotating ground-glass disk [31]. Thus, the image signal can be encoded into the spatial-coherence function of a partially coherent beam by following the approach shown in Eq. (1). The response function in Eq. (1) is set to be $H(\mathbf{r},\mathbf{v})=\tau(\mathbf{r})\exp(-ia_0\mathbf{r}\cdot\mathbf{v})$, where $\tau(\mathbf{r})$ is the amplitude of the partially coherent source and a_0 is a real factor that controls the spatial-coherence area of the source. Therefore, the cross-spectral density of the generated partially coherent source can be written as

$$W_s(\mathbf{r}_1,\mathbf{r}_2)=\tau^*(\mathbf{r}_1)\tau(\mathbf{r}_2)\mu_s(\mathbf{r}_1,\mathbf{r}_2), \quad (2)$$

where

$$\mu_s(\mathbf{r}_1,\mathbf{r}_2)=\iint P(\mathbf{v})\exp[ia_0(\mathbf{r}_1-\mathbf{r}_2)\cdot\mathbf{v}]d^2\mathbf{v}, \quad (3)$$

is the spatial degree of coherence of the partially coherent source [26], which is also termed the spatial-coherence structure [31]. Such a spatial degree of coherence changes during propagation. According to the reciprocal condition for partially coherent light, the far-field degree of coherence for a lowly spatially coherent source (i.e., a quasihomogeneous source [27]) is mainly determined by the Fourier transform of the source intensity [27], i.e., $\mu_f(\boldsymbol{\rho}_1,\boldsymbol{\rho}_2)\propto\mathcal{F}[|\tau(\mathbf{r})|^2]$, where the subscript f denotes the far field, $\boldsymbol{\rho}$ is the spatial position vector in the plane of the far field, and $\mathcal{F}$ denotes the Fourier transform. Thus, the image information encoded in $\mu_s(\mathbf{r}_1,\mathbf{r}_2)$ cannot be recovered by the far-zone spatial-coherence-structure measurement.

To maintain the distribution of the spatial degree of coherence in the far field, we introduce a cross phase into the cross-spectral density of the partially coherent source as follows [41–43]:

$$W_s(\mathbf{r}_1,\mathbf{r}_2)=\tau^*(\mathbf{r}_1)\tau(\mathbf{r}_2)\mu_s(\mathbf{r}_1,\mathbf{r}_2)\exp[-iu(x_1y_1-x_2y_2)], \quad (4)$$

where u is the real factor of the cross phase. The spatial distribution of the cross phase is shown in Fig. 1(a). In the following simulation, we find that when the factor u is sufficiently large (the value depends on the spatial-coherence area and the beam width of the partially coherent source), the far-field spatial degree of coherence is as follows:

$$\mu_f(\boldsymbol{\rho}_1,\boldsymbol{\rho}_2)\propto\mu_s(\mathbf{r}_1,\mathbf{r}_2). \quad (5)$$

Thus, the image information encoded ahead in $\mu_s(\mathbf{r}_1,\mathbf{r}_2)$ [Eq. (3)] can be transmitted to the spatial-coherence structure in the far field and the image information can be recovered from the far-field coherence measurement.

B. Propagation through transmission link

To show the robust feature of our coherence-based image transmission, we place a sector-shaped obstacle in the transmission path as shown in Fig. 1(a). The obstacle can move freely in the path. The distance between the obstacle and the partially coherent source is z'. The propagation of the partially coherent beam in the transmission link with the obstacle can be solved with the help of two generalized Huygens-Fresnel integrals [49]. The first and the second integrals are performed between the partially coherent source and the obstacle and the obstacle and the output plane, respectively. The spatial coordinates in the source plane, the obstacle plane, and the output plane are $\mathbf{r}$, $\boldsymbol{\rho}'$, and $\boldsymbol{\rho}$, respectively. The cross-spectral densities of the light fields in the obstacle plane and the output plane are written as $W'(\boldsymbol{\rho}'_1,\boldsymbol{\rho}'_2)$ and $W_{\mathrm{out}}(\boldsymbol{\rho}_1,\boldsymbol{\rho}_2)$. The averaged intensity and the spatial degree of coherence in the output plane can be obtained from

$$I_{\mathrm{out}}(\boldsymbol{\rho})=W_{\mathrm{out}}(\boldsymbol{\rho},\boldsymbol{\rho}), \quad (6)$$

$$\mu_{\mathrm{out}}(\boldsymbol{\rho}_1,\boldsymbol{\rho}_2)=\frac{W_{\mathrm{out}}(\boldsymbol{\rho}_1,\boldsymbol{\rho}_2)}{[I_{\mathrm{out}}(\boldsymbol{\rho}_1)I_{\mathrm{out}}(\boldsymbol{\rho}_2)]^{1/2}}. \quad (7)$$

C. Image recovery in the far field by spatial-coherence measurement

By following the relation set out in Eq. (5) as well as that in Eq. (3), it is found that the image information can be recovered in the far field by measuring the output spatial degree of coherence. Before discussing the measurement of $\mu_{\mathrm{out}}(\boldsymbol{\rho}_1,\boldsymbol{\rho}_2)$, we introduce the numerical approach to the output cross-spectral density calculation. The two generalized Huygens-Fresnel integrals used in partially coherent beam propagation cannot, in general, be solved analytically. By using the theory of the superposition of complex random screens [50–53], the cross-spectral density of a partially coherent source can be decomposed as the incoherent sum of N random modes, i.e.,

$$W_s(\mathbf{r}_1,\mathbf{r}_2) \simeq \frac{1}{N}\sum_{n=1}^{N} E_n^*(\mathbf{r}_1)E_n(\mathbf{r}_2), \tag{8}$$

where $E_n(\mathbf{r})$ is the nth random mode and it can be expressed as

$$E_n(\mathbf{r}) = \tau(\mathbf{r})\exp(iuxy)\mathcal{T}_n(\mathbf{r}). \tag{9}$$

Above, the random complex transmittance function of order n is obtained through $\mathcal{T}_n(\mathbf{r}) = \mathcal{F}[t_n(\mathbf{v})]$, where $t_n(\mathbf{v}) = \sqrt{P(\mathbf{v})}[a_n(\mathbf{v}) + ib_n(\mathbf{v})]$ is a complex random function, with $a_n(\mathbf{v})$ and $b_n(\mathbf{v})$ constituting two sets of real Gaussian random variables, each having unit variance and zero mean. The sets are independent in the sense that the variables in one set are independent of those in the other. The mode number N is closely related to the spatial-coherence area of the partially coherent source, i.e., the number increases with the decrease of the spatial-coherence area.

Thus, the propagation of the partially coherent beam in the transmission link can be solved with the help of the coherent-optics method. For the random mode of order n, the optical field just before the obstacle can be obtained through the following Fourier transform:

$$E_n'(\boldsymbol{\rho}') = \frac{ik}{2\pi B'}\exp\left(\frac{ikD'}{2B'}\boldsymbol{\rho}'^2\right) \times \mathcal{F}\left[E_n(\mathbf{r})\exp\left(\frac{ikA'}{2B'}\mathbf{r}^2\right)\right]\Bigg|_{\frac{\boldsymbol{\rho}'}{\lambda B'}}. \tag{10}$$

The corresponding optical field in the output plane can be obtained through

$$E_{n\,\mathrm{out}}(\boldsymbol{\rho}) = \frac{ik}{2\pi B}\exp\left(\frac{ikD}{2B}\boldsymbol{\rho}^2\right) \times \mathcal{F}\left[O(\boldsymbol{\rho}')E_n'(\boldsymbol{\rho}')\exp\left(\frac{ikA}{2B}\boldsymbol{\rho}'^2\right)\right]\Bigg|_{\frac{\boldsymbol{\rho}}{\lambda B}}, \tag{11}$$

where $O(\boldsymbol{\rho}')$ denotes the transmission function of the obstacle. By adding up the contributions from all the random modes, we obtain that the output cross-spectral density can be expressed as

$$W_{\mathrm{out}}(\boldsymbol{\rho}_1,\boldsymbol{\rho}_2) \simeq \frac{1}{N}\sum_{n=1}^{N} E_{n\,\mathrm{out}}^*(\boldsymbol{\rho}_1)E_{n\,\mathrm{out}}(\boldsymbol{\rho}_2). \tag{12}$$

We remark here that the optical field synthesized by the random modes shown in Eq. (9) obeys Gaussian statistics [54]. Thus, the (second-order) spatial degree of coherence has a well-defined relation with the (fourth-order) intensity correlation, i.e., [26]

$$g_{\mathrm{out}}(\boldsymbol{\rho}_1,\boldsymbol{\rho}_2) = 1 + |\mu_{\mathrm{out}}(\boldsymbol{\rho}_1,\boldsymbol{\rho}_2)|^2. \tag{13}$$

Above, $g_{\mathrm{out}}(\boldsymbol{\rho}_1,\boldsymbol{\rho}_2)$ is the normalized intensity-correlation function and can be obtained through

$$g_{\mathrm{out}}(\boldsymbol{\rho}_1,\boldsymbol{\rho}_2) = \frac{\langle I_{\mathrm{out}}(\boldsymbol{\rho}_1)I_{\mathrm{out}}(\boldsymbol{\rho}_2)\rangle}{\langle I_{\mathrm{out}}(\boldsymbol{\rho}_1)\rangle\langle I_{\mathrm{out}}(\boldsymbol{\rho}_2)\rangle}. \tag{14}$$

We now turn to discussing the measurement of the spatial degree of coherence in the far field. Typically, the spatial coherence can be measured with the help of Young's two-pinhole experiment [55,56]. However, the methods based on Young's interferometry have several limitations, e.g., low light efficiency and a long measurement time. The intensity-correlation measurement performed by the famous Hanbury Brown and Twiss (HBT) experiment, on the other hand, can overcome the above limitations [48].

However, it is found from the relation in Eq. (13) that only the modulus of the spatial degree of coherence can be recovered from the measurement of the intensity correlation. The phase information—which is quite important in image recovery, as shown in Eq. (3)—is missing. Although the phase information can be measured with the aid of the recently proposed generalized HBT experiment by introducing a pair of reference beams [57,58], the multiple measurements required in the experiment limit the real-time image recovery in this work.

Here, we apply the iterative phase-retrieval method [59,60] to recover the phase of the spatial degree of coherence and the information about the image signal. The principle is shown in Figs. 1(b) and 1(c). In the output plane of the transmission link, we record N intensity speckles generated by all the random modes. By using Eq. (14) and then Eq. (13), we obtain the modulus of the spatial degree of coherence $|\mu_{\mathrm{out}}(\boldsymbol{\rho}_1,\boldsymbol{\rho}_2)|$. To obtain the phase $\theta_{\mathrm{out}}(\boldsymbol{\rho}_1,\boldsymbol{\rho}_2)$ of the spatial degree of coherence, we first give an initial guess of the image signal $P_{k=1}(\mathbf{v})$. In this work, the guess of $P_{k=1}(\mathbf{v})$ is generated by a (real and non-negative) random function. We then carry out the Fourier transform of the guess function to obtain the corresponding spatial degree of coherence $\mu_{k=1}(\boldsymbol{\rho}_1,\boldsymbol{\rho}_2)$. We extract the phase $\theta_{k=1}(\boldsymbol{\rho}_1,\boldsymbol{\rho}_2)$ and combine it with the modulus of the measured spatial degree of coherence $|\mu_{\mathrm{out}}(\boldsymbol{\rho}_1,\boldsymbol{\rho}_2)|$. By doing the inverse Fourier transform of the generated spatial degree of coherence $\mu_{k=1}'(\boldsymbol{\rho}_1,\boldsymbol{\rho}_2) = |\mu_{\mathrm{out}}(\boldsymbol{\rho}_1,\boldsymbol{\rho}_2)|e^{i\theta_{k=1}(\boldsymbol{\rho}_1,\boldsymbol{\rho}_2)}$, we obtain $P_{k=1}'(\mathbf{v})$, which is in general a complex function. In the next step, the negative and complex values in $P_{k=1}'(\mathbf{v})$ are replaced with 0 (error-reduction algorithm) or $P_{k=1}(\mathbf{v}) - \beta P_{k=1}'(\mathbf{v})$ (hybrid input-output algorithm) [61,62], where β is a feedback parameter that controls the convergence properties of the algorithm. The output function then replaces the initial guess function and we perform the above steps again. In our simulation, we start with the hybrid input-output algorithm and gradually lower β from 2 to 0, with a step length of 0.05. We run ten iterations per value of β. After that, we run 100 iterations with the error-reduction algorithm to reduce any residual noise from the output image. One of the output results for the recovered image $P_{\rm out}(\mathbf{v})$ is shown in Fig. 1(b).

III. SIMULATION RESULTS

To conveniently show the far-field information for the intensity and the degree of coherence, we place a thin lens of focal distance f immediately after the partially coherent source. The far-field information thus can be obtained in the focal plane of the lens. The optical transfer matrices for the two systems are expressed as

$$\begin{pmatrix} A' & B' \\ C' & D' \end{pmatrix} = \begin{pmatrix} 1-z'/f & z' \\ -1/f & 1 \end{pmatrix}, \tag{15}$$

$$\begin{pmatrix} A & B \\ C & D \end{pmatrix} = \begin{pmatrix} 1 & f-z' \\ 0 & 1 \end{pmatrix}. \tag{16}$$

In the simulation, the focal distance of the thin lens is $f = 250$ mm. The image information $P(\mathbf{v})$ is a letter "S" as shown in Fig. 1(a). Other different images are also used in our simulation to check the robustness of our protocol. To ensure convergence of the random-mode superposition method, $N = 5000$ random modes are used for the partially coherent sources with different spatial-coherence areas. The recorded intensity of each random mode in the focal plane can be used to calculate the averaged intensity distribution and the modulus of the spatial degree of coherence in the far field. The image information can then be recovered by following the iterative phase-retrieval method introduced above. Other parameters used in the simulation are $u = 60$ mm^{-2}, $\lambda = 532$ nm, and $\tau(\mathbf{r}) = \exp(-\mathbf{r}^2/4\omega_0^2)$, with $\omega_0 = 1$ mm.

A. Intensity distribution

We first show, in Fig. 2, the intensity distribution of partially coherent beam propagation in the transmission link. The simulation results shown in the top panel of Fig. 2 are the intensities at different propagation distances when the obstacle is removed. We find that the intensity can reconstruct its Gaussian spot in the focal plane. This is due to the effect of the cross phase [43]. We note that during propagation, the beam shows a strong shear along the diagonal direction [Fig. 2(b)]. This is because the cross phase shows a jump of π between the diagonal and the antidiagonal directions [see Fig. 1(a)]. With the decrease of the value of the phase factor u, we find that the Gaussian spot in the focal plane is distorted (not shown here). We find in the second row of Fig. 2 that when the obstacle is present in the source plane, the focal-plane intensity is a combination of the Gaussian spot and the obstacle. It can also be regarded as the reconstruction of the initial intensity. In such a case, the effect of the obstacle cannot be removed. In the third row of Fig. 2, we display more results for the focal-plane intensity with different shapes of obstacle placed at the source. In the bottom panel of Fig. 2, we show the simulation results for the intensity distribution in the focal plane for the case when the obstacle with sector angle $\alpha = \pi$ is placed at different places in the transmission link. The results confirm the effect of the obstacle on the focal-plane intensity distribution. All the simulation results in Fig. 2 indicate that the intensity cannot be used to robustly transmit the image signal when the obstacle is present in the transmission link.

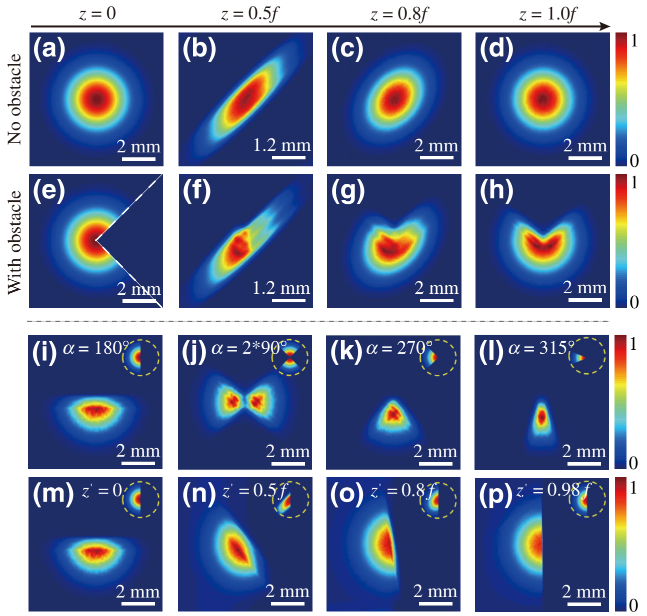

FIG. 2. The simulation results for the normalized intensity distributions of partially coherent beam propagation in the transmission link. (a)–(d) The intensity distributions at different propagation distances with no obstacle within the propagation link. (e)–(h) The intensity distributions at different propagation distances with the sector-shaped obstacle within the propagation link. (i)–(l) The intensity distributions in the focal plane for the obstacles placed at the source with different sector angles α. (m)–(p) The intensity distributions in the focal plane for the obstacle with sector angle $\alpha = \pi$ placed at different places having a distance z' from the source plane.

We remark here that when the cross phase is removed from the source plane, the far-field intensity can reconstruct the shape of the image signal when the spatial-coherence area of the partially coherent source is sufficiently low and the obstacle is placed in the source plane or removed [47]. This is due to the reciprocal condition for partially coherent light, i.e., $I_{\rm out}(\boldsymbol{\rho}) \propto \mathcal{F}[\mu_s(\mathbf{r}_1, \mathbf{r}_2)] \propto P(\mathbf{v})$ [27]. However, as shown in the bottom panel of

Fig. 2, the image signal is distorted when the obstacle is placed in other places within the transmission link. Thus, we conclude that the intensity cannot robustly transmit the image information.

B. Spatial degree of coherence and recovered image

We now turn to checking the robustness of the spatial degree of coherence in the focal plane. In Fig. 3(a), we show the spatial distribution of $|\mu_{\text{out}}(\boldsymbol{\rho}_1, \boldsymbol{\rho}_2)|$ in the focal plane for the case when the obstacle is removed from the transmission link. Figure 3(e) shows the corresponding result for the recovered image obtained by the phase-retrieval algorithm. We see that the spatial-coherence structure of the partially coherent random light can indeed be used to transmit the image signal to the focal plane (or the far field). In Figs. 3(b)–3(d), we display the simulation results for the cases when obstacles with different sector angles are present in the source plane. Figures 3(f)–3(h) show the corresponding results for the recovered image. It is found that in the presence of the obstacle, even with only a 90° open angle, the image can still be recovered in the focal plane. This property shows the robustness of the spatial-coherence structure for image transmission. However, in Figs. 3(d) and 3(h), we find when the opening of the obstacle is very small, the output image signal is distorted. This is because in such cases, the spatial-coherence area (approximately 0.5^2 mm^2) of the partially coherent source is larger than the opening area of the obstacle (see the discussion in Sec. III D). Thus, by further decreasing the spatial-coherence area of the partially coherent source, the image signal can still be recovered (see the simulation results in Fig. 5).

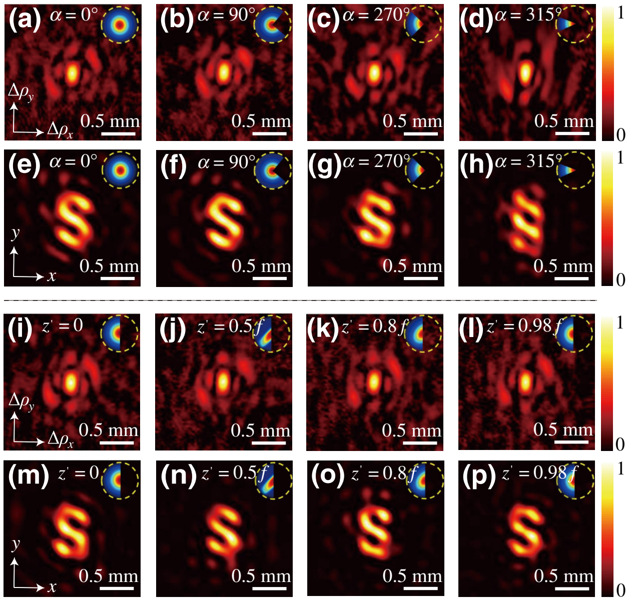

FIG. 3. The simulation results for the modulus of the spatial degree of coherence in the focal plane and the corresponding results for the recovered image. (a),(e) The simulation results for the case when the obstacle is removed. (b)–(d),(f)–(h) The simulation results for the cases when obstacles with different sector angles α are placed in the source plane. (i)–(l),(m)–(p) The simulation results for the obstacle with sector angle $\alpha = \pi$ placed at different positions at distance z' from the source plane.

We now study the situation when the obstacle is placed inside of the propagation channel. In Figs. 3(i)–3(l), we show the spatial distributions of the focal-plane degree of coherence and in Figs. 3(m)–3(p) we show the corresponding recovered images for the cases when the obstacle with sector angle $\alpha = \pi$ is placed at different positions in the transmission link. From the simulation results, we can conclude that the spatial degree of coherence in the focal plane is effectively independent of the position of the obstacle in the transmission link and that the spatial-coherence structure can be used for robustly transmitting an optical image to the far field.

C. Transmission with different images and different obstacles

To check the broad applicability of our protocol, we replace the letter “S” with different images, i.e., arabic numerals from 0 to 9. The initial images $P(\mathbf{v})$ and the corresponding modulus of the spatial degree of coherence $|\mu_s(\mathbf{r}_1, \mathbf{r}_2)|$ for the partially coherent sources are shown in Figs. 4(a) and 4(b). The simulated results for the modulus of the spatial degree of coherence $|\mu_{\text{out}}(\boldsymbol{\rho}_1, \boldsymbol{\rho}_2)|$ in the output plane are shown in Fig. 4(c). By using the iterative phase-retrieval algorithm, we obtain the recovered images, which are shown in Figs. 4(d). From the simulation results in Fig. 4, we find that different images can be recovered well in the focal plane (or far field), which indicates the broad applicability of our protocol for different image shapes. We note here that the spatial distribution of $|\mu_{\text{out}}(\boldsymbol{\rho}_1, \boldsymbol{\rho}_2)|$ rotates by 90° compared to $|\mu_s(\mathbf{r}_1, \mathbf{r}_2)|$ [see also the intensity in Figs. 2(e) and 2(f)]. This is due to the particular distribution of the orbital-angular-momentum flux density induced by the cross phase [63], which introduces rotation in the cross-spectral density of a partially coherent beam. It is also remarkable that our protocol works well for the recovery of binary images. However, the grayscale images are hard to recover (the simulation results are not shown here), as this is challenging for the phase-retrieval algorithm [61,62].

We now place the obstacles with different shapes in the source plane and check whether the recovered image is affected by the shapes of the obstacles. The intensities of the partially coherent beam passing through the obstacles are shown in Figs. 5(a)–5(d). In Fig. 5(a), the opening of the obstacle forms a circular ring. Thus, the field at the center and the edge is blocked. In Figs. 5(b), 5(c), and 5(d), the obstacles with circular, rectangular, and triangular openings are placed at different transverse locations in the

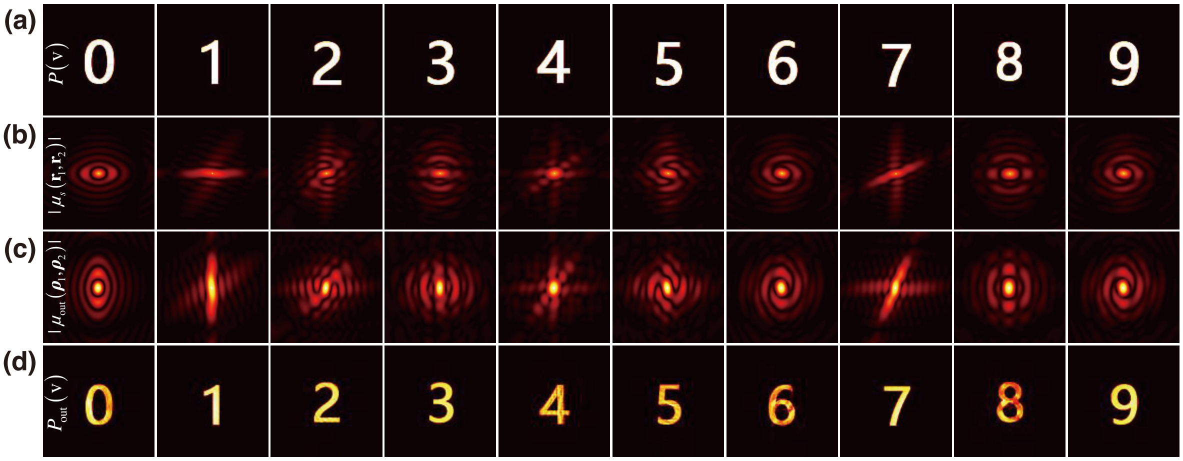

FIG. 4. (a) Different original images $P(\mathbf{v})$. (b) The distributions of the modulus of the spatial degree of coherence $|\mu_s(\mathbf{r}_1,\mathbf{r}_2)|$ of the corresponding generated partially coherent sources. (c) The corresponding distributions of the modulus of the spatial degree of coherence $|\mu_{\text{out}}(\boldsymbol{\rho}_1,\boldsymbol{\rho}_2)|$ in the output plane. (d) The recovered images $P_{\text{out}}(\mathbf{v})$ with the iterative phase-retrieval algorithm.

source plane. Figures 5(e)–5(h) show the corresponding distributions for the spatial degree of coherence in the output plane, while Figs. 5(i)–5(l) display the recovered images with the iterative phase-retrieval algorithm. It is found that in all the cases, the images can be recovered well in the far field and the image quality is effectively independent of the shape of the obstacle. The reason behind this is that in Fig. 5, the spatial-coherence area of the partially coherent source is matched well with (comparable to) the opening area of the obstacles, which is discussed in the following subsection.

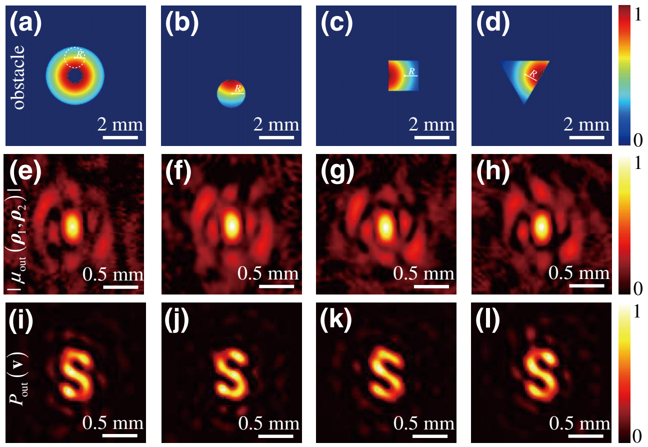

FIG. 5. Simulation results for the effect of the shape and location of the obstacle on the recovered image quality. (a)–(d) The intensity distributions of the light passing through the obstacles with the circular ring, off-axis circular, rectangular, and triangular openings, respectively. (e)–(h) The corresponding distributions of the modulus of the spatial degree of coherence in the output plane. (i)–(l) The corresponding recovered images from (e)–(h).

D. Effect of spatial-coherence area

To check the effect of the spatial-coherence area of the partially coherent source on the output image quality, we consider two situations. In the first situation, the spatial-coherence area of the partially coherent source is fixed, while the opening size of the obstacle changes. In the second situation, the opening size of the obstacle is fixed, but the spatial-coherence area of the partially coherent source changes in relation to the image size.

In Fig. 6, we show the simulation results for the first case. In the simulation, the obstacle is replaced with a circular pinhole with radius R that changes from 0 to 3 mm [see Fig. 6(b)]. The obstacle is placed in the source plane. Figure 6(a) shows the spatial distribution of the degree of coherence for the partially coherent source. We see that the initial spatial-coherence length $\delta_0 \approx 0.5$ mm and that the spatial-coherence area is about 0.5^2 mm^2. Figures 6(c) and 6(d) show the spatial degree of coherence in the focal plane and the corresponding result for the recovered image when the obstacle is removed. We now put the obstacle after the partially coherent source and calculate the spatial degree of coherence $\mu'_{\text{out}}(\Delta\boldsymbol{\rho})$ in the focal plane. Figure 6(o) illustrates the similarity (gray stars) between the recovered images and the original "S" image [Fig. 6(p)]. The similarity is defined as [9]

$$S = \frac{\iint |P_{\text{out}}(\mathbf{v}) - \overline{P}_{\text{out}}||P(\mathbf{v}) - \overline{P}|d^2\mathbf{v}}{[\iint |P_{\text{out}}(\mathbf{v})|^2 d^2\mathbf{v} \iint |P(\mathbf{v})|^2 d^2\mathbf{v}]^{1/2}}. \tag{17}$$

Above, $\overline{P}$ and $\overline{P}_{\text{out}}$ denote the averaged intensities for the original and recovered images, respectively. The value of S is bounded as $0 < S \leq 1$. The larger value of S represents more identity between the recovered image $P_{\text{out}}(\mathbf{v})$ and the original image $P(\mathbf{v})$. From the simulation results in Fig. 6(o), we find that with the increase of the opening

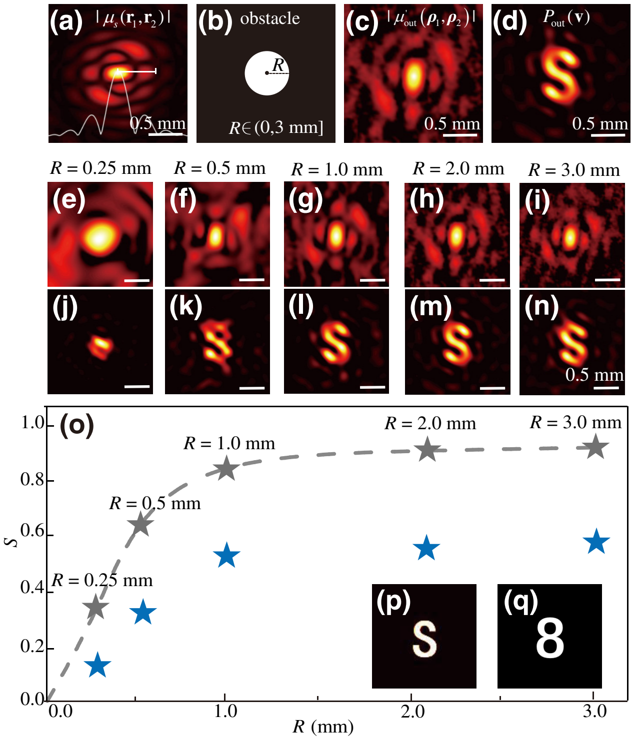

FIG. 6. Simulation results for the effect of the obstacle size on the recovered image quality. (a) The distribution of the modulus of the spatial degree of coherence in the source plane. (b) The obstacle with a circular opening of radius R ranging from 0 to 3 mm. (c) The distribution of the modulus of the spatial degree of coherence in the output plane when the obstacle is removed. (d) The recovered image from the distribution in (c). (e)–(i) The distributions of the modulus of the spatial degree of coherence in the output plane with the obstacle having radius $R = 0.25$ mm, 0.5 mm, 1.0 mm, 2.0 mm, and 3.0 mm, respectively. (j)–(n) The corresponding recovered images from (e)–(i). (o) The similarities S between the recovered images and the original image "S" [see (p)] (gray stars) and between the recovered images and the image "8" [see (q)] (blue stars) as a function of the radius R.

area of the obstacle, the recovered images become more and more similar to the original ones. Figures 6(e)–6(n) show the output degrees of coherence and the corresponding recovered images for radius $R = 0.25$ mm, 0.5 mm, 1.0 mm, 2.0 mm, and 3.0 mm. We find that when the opening area of the obstacle is comparable with or larger than the spatial-coherence area of the partially coherent source, the image information can be recovered well. With the increase of the opening area, the image quality becomes better. However, when the opening area is smaller than the spatial-coherence area, the image signal cannot be identified [see Figs. 6(e) and 6(j)]. The reason behind this can be found in Fig. 6(e), i.e., most of the high-frequency components of the image (located at the edge of the spatial distribution of the coherence) are lost in the far field for a small opening of the obstacle. To further see the performance of our algorithm, we show the similarity between the recovered images shown in Figs. 6(j)–6(n) and the image "8" shown in Fig. 6(q). The simulation results are shown in Fig. 6(o) (blue stars). It is found that the similarity between the recovered images and the image "8" is always smaller than that for the original image "S," which indicates the good performance of our algorithm.

In Fig. 7, we show the simulation results for the second case. In this case, the radius R is fixed at 0.7 mm, while the spatial-coherence width δ_0 varies from 0.2 mm to 1.2 mm. The spatial-coherence width of the partially coherent source can be altered by controlling the parameter a_0 in the $H(\mathbf{r},\mathbf{v})$ function. The top panel of Fig. 7 shows the distributions of the spatial degree of coherence in the source plane, while Figs. 7(g)–7(k) show the distributions of the spatial degree of coherence in the focal plane. In Figs. 7(l)–7(p), we display the recovered images from $|\mu_{\rm out}(\Delta\boldsymbol{\rho})|$. The similarity between the recovered images and the original image are displayed in Fig. 7(f).

As expected, when the spatial-coherence area of the partially coherent source is comparable to (or smaller than) the opening area of the obstacle, the output image can be recovered well [Figs. 7(m), 7(n), and 7(o)]. However, when the spatial-coherence area continues to increase (larger than the opening area of the obstacle), the recovered image quality will be distorted [see Fig. 7(p)]. More surprisingly, with the decrease of the spatial-coherence area and when its value becomes smaller than the opening area of the

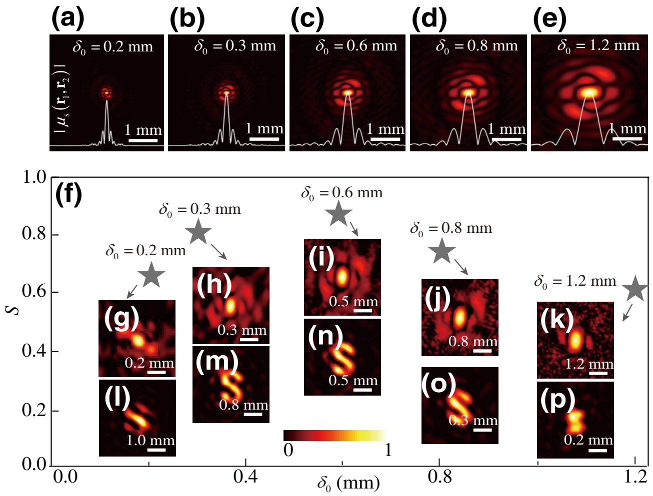

FIG. 7. Simulation results for the effect of the initial spatial-coherence area of the partially coherent source on the recovered image quality. (a)–(e) The distributions of the modulus of the spatial degree of coherence in the source plane for the partially coherent sources with different initial spatial-coherence widths δ_0. (g)–(k) The distribution of the modulus of the spatial degree of coherence in the output plane for the case when the obstacle with the opening radius $R = 0.7$ mm is placed in the source plane. (l)–(p) The corresponding recovered images from (g)–(k). (f) The similarity S between the recovered image and the original image as a function of the initial spatial-coherence width δ_0.

obstacle, the similarity between the recovered image and the original image also decreases [see Fig. 7(l)]. This can be explained as follows: the large feature of the image cannot be resolved at the low spatial-coherence length of the partially coherent source. Thus, we can conclude that for an optimal image output, the spatial-coherence area of the partially coherent source, the opening area of the obstacle, and the image size must be matched well, i.e., the spatial-coherence area must be smaller than (or comparable to) the opening area, but larger than (or comparable to) the image size [see, e.g., Fig. 7(n)].

IV. EXPERIMENTAL VERIFICATION

We now carry out a proof-of-principle experiment to show the robustness of the spatial-coherence structure in the far-field image transmission. Figure 8 shows the experimental setup for encoding an image signal into the spatial-coherence structure of the partially coherent random light beam, propagation of the light field in the transmission link with an obstacle, and the focal-plane spatial-coherence measurement.

A fully coherent light beam, created by transmitting a Nd:YAG laser of wavelength $\lambda = 532$ nm through a neutral density filter (NDF) and a beam expander (BE), is impinged onto a spatial light modulator (SLM) with the image signal (the letter “S”) loaded on it. The image signal $P(\mathbf{v})$ is projected onto a rotating ground glass disk (RGGD) by a $2f$ imaging system composed of a thin lens L_1 of focal distance $f_1 = 150$ mm. The distances between the SLM and the L_1 and between the L_1 and the RGGD are both equal to $2f_1$. The light beam transmitted by a RGGD can be regarded as an incoherent secondary source since the beam-spot size on the RGGD is much larger than the characteristic inhomogeneity scale of the RGGD [64]. The cross-spectral density of the incoherent light is given by $W(\mathbf{v}_1, \mathbf{v}_2) = P(\mathbf{v}_1)\delta(\mathbf{v}_1 - \mathbf{v}_2)$, where $\delta(\cdot)$ is a Dirac delta function. After the emerging incoherent beam passes through a thin lens L_2 of focal length $f_2 = 250$ mm and a Gaussian amplitude filter (GAF), the partially coherent light source is generated, with its spatial degree of coherence expressed as

$$\mu_s(\mathbf{r}_1, \mathbf{r}_2) = 1/(\lambda f_2)^2 \int d^2\mathbf{v} P(\mathbf{v}) \times \exp[i2\pi(\mathbf{r}_1 - \mathbf{r}_2) \cdot \mathbf{v}/(\lambda f_2)]. \tag{18}$$

We note here that the partially coherent source generated in this manner has a statistically homogeneous spatial degree of coherence and obeys Gaussian statistics, since it is generated by an incoherent source from a RGGD [31,64]. The role of the GAF is used to shape the intensity of the partially coherent source into an effectively uniform distribution. To embed a cross phase into the partially coherent source, a phase-only SLM is placed immediately after the source. The computer-generated hologram loaded in the SLM is shown in the inset of Fig. 8. The reflected light beam from the SLM passes through a $4f$ optical system that consists of thin lenses L_3 and L_4, with the focal distance being 100 mm. A circular aperture (CA) is placed at the Fourier plane of the $4f$ system to filter out the first-order diffraction pattern of the light from the SLM. In the rear focal plane of L_4, a partially coherent beam having the cross-spectral density shown in Eq. (4) is generated. We then transmit the partially coherent beam in the transmission link composed of a thin lens L_5 with focal distance $f_5 = 250$ mm and a sector-shaped obstacle with controllable sector angle α. In the output plane, a charge-coupled device (CCD) is used to record the intensity speckles. In our experiment, 5000 random realizations are recorded by the CCD. The modulus of the spatial degree of coherence $|\mu_{\text{out}}(\boldsymbol{\rho}_1, \boldsymbol{\rho}_2)|$ and the image signal can be obtained from the realizations by using the method we discuss in Sec. III C. We note that the RGGD rotates slowly in our experiment to ensure that the CCD, with an integration time of 20 ms and a frame rate of 30 frames/s, can capture all the realizations.

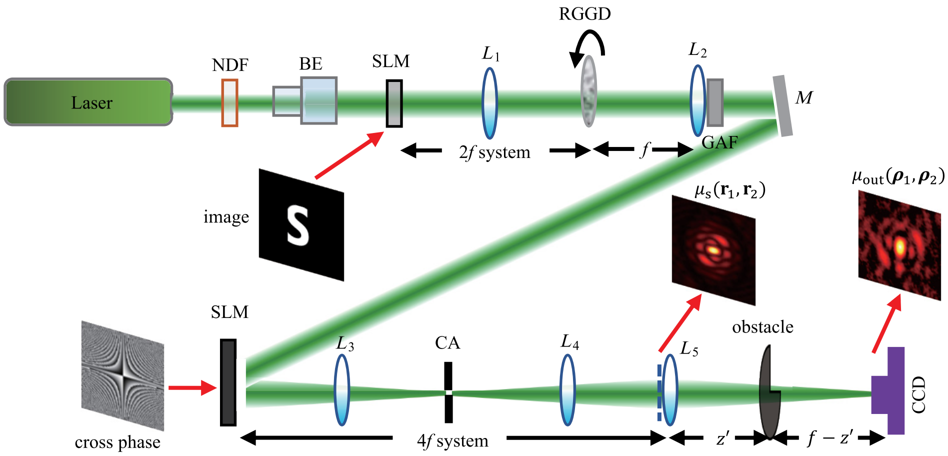

FIG. 8. The experimental setup for far-field robust image transmission with partially coherent random light beams: NDF, neutral density filter; BE, beam expander; SLM, spatial light modulator; RGGD, rotating ground-glass disk; L_1, L_2, L_3, L_4, and L_5, thin lenses; GAF, Gaussian amplitude filter; M, mirror; CA, circular aperture; CCD, charge-coupled device. We note that the distance between the GAF and the SLM is very short.

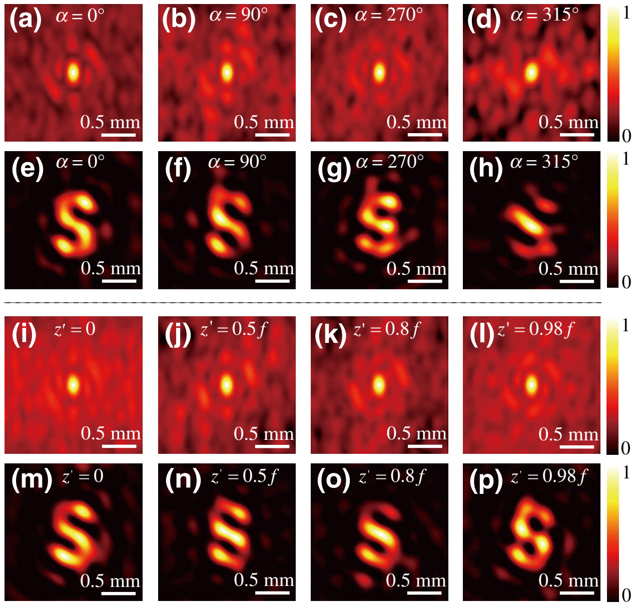

FIG. 9. Experimental results for the measured modulus of the spatial degree of coherence in the focal plane and the corresponding results for the recovered image. (a),(e) The experimental results for the case when the obstacle is removed. (b)–(d),(f)–(h) The experimental results for the cases when obstacles with different sector angles α are placed in the source plane. (i)–(l),(m)–(p) The experimental results for the obstacle with sector angle $\alpha = \pi$ placed at different positions at distance z' from the source plane.

In the experiment, obstacles with different sector angles are first placed in the source plane of the partially coherent beam. The experimental results for the modulus of the spatial degree of coherence in the output plane are shown in Figs. 9(a)–9(d). The corresponding recovered images are shown in Figs. 9(e)–9(h). First of all, we find in the experimental results that the spatial-coherence structure of a partially coherent random light beam can indeed be used for robustly transmitting the image signal in the transmission link with obstacles. Second, the output image quality depends on the opening area of the obstacle and the spatial-coherence area of the partially coherent source. When the spatial-coherence area is smaller than or comparable to the opening area, the image information can be recovered well. On the contrary, the image information is distorted when the spatial-coherence area is larger than the opening area. The results indicate the superiority of the spatial-coherence engineering in the image information transmission.

Next, we move the obstacle with sector angle $\alpha = 180°$ from the source plane to other locations in the transmission link. The experimental results for the measured modulus of the spatial degree of coherence in the output plane are shown in Figs. 9(i)–9(l) and the corresponding recovered images are displayed in Figs. 9(m)–9(p). The experimental results are consistent with our prediction that wherever the obstacle is placed in the transmission link, the image can be recovered well in the output plane. The behavior of the spatial-coherence structure is different from that for the intensity distribution in the output plane, as we show in Fig. 2. This indicates that the second-order (two-point) spatial-coherence structure can be viewed as a robust parameter to transmit the image information.

V. CONCLUSIONS

In summary, we study the far-field image information transmission with modulation of the spatial-coherence structure of a partially coherent random beam. We give in detail the principle and the theoretical background of the coherence-based image encoding, transmission, and recovery. The evolution of the spatial-coherence-structure propagation in the transmission link with different obstacles has been simulated with the random-mode-decomposition theory. The effects of the shape, size, and position of the obstacle, as well as the spatial-coherence area of the partially coherent source on the output image quality, are discussed. It is found that when the spatial-coherence area is smaller than or comparable to the opening area of the obstacle (but is larger than or comparable to the image size) and wherever the obstacle is placed in the transmission link, the image signal can be recovered well in the far field. A proof-of-principle experiment is carried out to show the robustness of the second-order spatial-coherence structure in far-field image transmission.

Our results provide an efficient tool for optical information transmission in the complex environment and may find further application in turbulence-free optical communications. We remark that to realize coherence-based optical image transmission in turbulent atmospheres, the random realizations for synthesizing a partially coherent source must be generated rapidly, i.e., the time scale must be shorter than the characteristic time for the fluctuations in the turbulence, and the camera used for capturing the random realizations must have an exposure time much shorter than the characteristic time of the turbulence [65]. The speed of the generation of the random realizations could be helpful with regard to the ultrafast modulator, e.g., a digital micromirror device [66,67]. Meanwhile, a single-photon detector array with an ultrafast response can be used as the camera. Finally, we remark that although the transmitted image studied in this work is an amplitude signal, a complex image (including the amplitude and phase as well as the polarization information) can be transmitted by using a similar protocol in which the scalar random source is replaced with an electromagnetic partially coherent source [27,48,58].

ACKNOWLEDGMENTS

This work was supported by the National Natural Science Foundation of China (NSFC) (Grants No. 91750201, No. 11974218, No. 11874046, No. 11904247, and No. 12192254); the National Key Research and Development

Project of China (Grant No. 2019YFA0705000); the Innovation Group of Jinan (Grant No. 2018GXRC010); and the Local Science and Technology Development Project of the Central Government (Grant No. YDZX20203700001766).

[1] H. Kaushal, V. K. Jain, and S. Kar, *Free Space Optical Communication* (Springer, New Dehli, 2017).

[2] X. Zhu and J. M. Kahn, Free-space optical communication through atmospheric turbulence channels, IEEE Trans. Commun. **50**, 1293 (2002).

[3] S. M. Popoff, G. Lerosey, M. Fink, A. C. Boccara, and S. Giganr, Image transmission through an opaque material, Nat. Commun. **1**, 1 (2010).

[4] L. Andrews and R. Phillips, *Laser Beam Propagation through Random Media* (SPIE, Bellinghan, 2005), 2nd ed.

[5] J. Broky, G. A. Siviloglou, A. Dogariu, and D. N. Christodoulides, Self-healing properties of optical Airy beams, Opt. Express **16**, 12880 (2008).

[6] Y. Liang, Y. Hu, D. Song, C. Lou, X. Zhang, Z. Chen, and J. Xu, Image signal transmission with Airy beams, Opt. Lett. **40**, 5686 (2015).

[7] G. Zhu, Y. Wen, X. Wu, Y. Chen, J. Liu, and S. Yu, Obstacle evasion in free-space optical communications utilizing Airy beams, Opt. Lett. **43**, 1203 (2018).

[8] A. E. Willner, H. Huang, Y. Yan, Y. Ren, N. Ahmed, G. Xie, C. Bao, L. Li, Y. Cao, and Z. Zhao *et al.*, Optical communications using orbital angular momentum beams, Adv. Opt. Photon. **7**, 66 (2015).

[9] W. Lin, Y. Wen, Y. Chen, Y. Zhang, and S. Yu, Resilient Free-Space Image Transmission with Helical Beams, Phys. Rev. Appl. **12**, 044058 (2019).

[10] W. Cheng, J. W. Haus, and Q. Zhan, Propagation of vector vortex beams through a turbulent atmosphere, Opt. Express **17**, 17829 (2009).

[11] G. Wu, F. Wang, and Y. Cai, Generation and self-healing of a radially polarized Bessel-Gauss beam, Phys. Rev. A **89**, 043807 (2014).

[12] M. A. Cox, C. Rosales-Guzmán, M. P. J. Lavery, D. J. Versfeld, and A. Forbes, On the resilience of scalar and vector vortex modes in turbulence, Opt. Express **24**, 18105 (2016).

[13] J. W. Goodman, *Speckle Phenomena in Optics: Theory and Applications* (Roberts and Company, Greenwood Village, CO, 2007).

[14] A. I. Kon and V. I. Tatarskii, On the theory of propagation of partially coherent light beams in a turbulent atmosphere, Radiophys. Quantum Electron. **15**, 1187 (1972).

[15] M. S. Belen'kii, A. I. Kon, and V. L. Mironov, Turbulent distortions of the spatial coherence of a laser beam, Sov. J. Quantum Electron. **7**, 287 (1977).

[16] J. C. Leader, Atmospheric propagation of partially coherent radiation, J. Opt. Soc. Am. **68**, 175 (1978).

[17] R. L. Fante, Two-position, two-frequency mutual-coherence function in turbulence, J. Opt. Soc. Am. **71**, 1446 (1981).

[18] J. C. Leader, Intensity fluctuations resulting from partially coherent light propagating through atmospheric turbulence, J. Opt. Soc. Am. **69**, 73 (1979).

[19] J. C. Ricklin and F. M. Davidson, Atmospheric turbulence effects on a partially coherent Gaussian beam: Implications for free-space laser communication, J. Opt. Soc. Am. A **19**, 1794 (2002).

[20] J. C. Ricklin and F. M. Davidson, Atmospheric optical communication with a Gaussian Schell beam, J. Opt. Soc. Am. A **20**, 856 (2003).

[21] Y. Liu, Y. Chen, F. Wang, Y. Cai, C. Liang, and O. Korotkova, Robust far-field imaging by spatial coherence engineering, Opto-Electron. Adv. **4**, 210027 (2021).

[22] B. Redding, M. Choma, and H. Cao, Speckle-free laser imaging using random laser illumination, Nat. Photonics. **6**, 355 (2012).

[23] Y. Eliezer, G. Qu, W. Yang, Y. Wang, H. Yilmaz, S. Xiao, Q. Song, and H. Cao, Suppressing meta-holographic artifacts by laser coherence tuning, Light Sci. Appl. **10**, 104 (2021).

[24] J. N. Clark, X. Huang, R. Harder, and I. K. Robinson, High-resolution three-dimensional partially coherent diffraction imaging, Nat. Commun. **3**, 1 (2012).

[25] X. Lu, Y. Shao, C. Zhao, S. Konijnenberg, X. Zhu, Y. Tang, Y. Cai, and H. Urbach, Noniterative spatially partially coherent diffractive imaging using pinhole array mask, Adv. Photon **1**, 016005 (2019).

[26] L. Mandel and E. Wolf, *Optical Coherence and Quantum Optics* (Cambridge University, Cambridge, 1995).

[27] E. Wolf, *Introduction to the Theory of Coherence and Polarization of Light* (Cambridge University Press, Cambridge, 2007).

[28] F. Wang, Y. Chen, X. Liu, Y. Cai, and S. A. Ponomarenko, Self-reconstruction of partially coherent light beams scattered by opaque obstacles, Opt. Express **24**, 23735 (2016).

[29] X. Liu, X. Peng, L. Liu, G. Wu, C. Zhao, F. Wang, and Y. Cai, Self-reconstruction of the degree of coherence of a partially coherent vortex beam obstructed by an opaque obstacle, Appl. Phys. Lett. **110**, 181104 (2017).

[30] X. Peng, H. Wang, L. Liu, F. Wang, S. Popov, and Y. Cai, Self-reconstruction of twisted Laguerre-Gaussian Schell-model beams partially blocked by an opaque obstacle, Opt. Express **28**, 31510 (2020).

[31] Y. Cai, Y. Chen, J. Yu, X. Liu, and L. Liu, Generation of partially coherent beams, Prog. Opt. **62**, 157 (2017).

[32] Y. Chen, A. Norrman, S. A. Ponomarenko, and A. T. Friberg, Optical coherence and electromagnetic surface waves, Prog. Opt. **65**, 105 (2020).

[33] O. Korotkova and G. Gbur, Applications of optical coherence theory, Prog. Opt. **65**, 43 (2020).

[34] Z. Zalevsky, J. García, P. García-Martínez, and C. Ferreira, Spatial information transmission using orthogonal mutual coherence coding, Opt. Lett. **30**, 2837 (2005).

[35] V. Micó, J. García, C. Ferreira, D. Sylman, and Z. Zalevsky, Spatial information transmission using axial temporal coherence coding, Opt. Lett. **32**, 736 (2007).

[36] C. Liang, G. Wu, F. Wang, W. Li, Y. Cai, and S. A. Ponomarenko, Overcoming the classical Rayleigh diffraction limit by controlling two-point correlations of partially coherent light sources, Opt. Express **25**, 28352 (2017).

[37] Y. Shen, H. Sun, D. Peng, Y. Chen, Q. Cai, D. Wu, F. Wang, Y. Cai, and S. A. Ponomarenko, Optical image

reconstruction in 4*f* imaging system: Role of spatial coherence structure engineering, Appl. Phys. Lett. **118**, 181102 (2021).

[38] Y. Chen, S. A. Ponomarenko, and Y. Cai, Experimental generation of optical coherence lattices, Appl. Phys. Lett. **109**, 061107 (2016).

[39] D. Peng, Z. Huang. Y. Liu, Y. Chen, F. Wang, S. A. Ponomarenko, and Y. Cai, Optical coherence encryption with structured random light, PhotoniX **2**, 1 (2021).

[40] W. H. Carter and E. Wolf, Coherence and radiometry with quasihomogeneous planar sources, J. Opt. Soc. Am. A **67**, 785 (1977).

[41] R. Simon and N. Mukunda, Twisted Gaussian Schell-model beams, J. Opt. Soc. Am. A **10**, 95 (1993).

[42] R. Simon and N. Mukunda, Twist phase in Gaussian-beam optics, J. Opt. Soc. Am. A **15**, 2373 (1998).

[43] R. Pan, X. Liu, J. Tang, H. Ye, Z. Liu, P. Ma, W. Wen, B. J. Hoenders, Y. Cai, and C. Liang, Enhancing the self-reconstruction ability of the degree of coherence of a light beam via manipulating the cross-phase structure, Appl. Phys. Lett. **119**, 111105 (2021).

[44] F. Gori and M. Santarsiero, Devising genuine spatial correlation functions, Opt. Lett. **32**, 3531 (2007).

[45] R. Martínez-Herrero, P. M. Mejías, and F. Gori, Genuine cross-spectral densities and pseudo-modal expansions, Opt. Lett. **34**, 1399 (2009).

[46] S. Sahin and O. Korotkova, Light sources generating far fields with tunable flat profiles, Opt. Lett. **37**, 2970 (2012).

[47] F. Wang, X. Liu, Y. Yuan, and Y. Cai, Experimental generation of partially coherent beams with different complex degrees of coherence, Opt. Lett. **38**, 1814 (2013).

[48] Y. Chen, F. Wang, L. Liu, C. Zhao, Y. Cai, and O. Korotkova, Generation and propagation of a partially coherent vector beam with special correlation functions, Phys. Rev. A **89**, 013801 (2014).

[49] S. A. Collins, Jr., Lens-system diffraction integral written in terms of matrix optics, J. Opt. Soc. Am. **60**, 1168 (1970).

[50] D. Voelz, X. Xiao, and O. Korotkova, Numerical modeling of Schell-model beams with arbitrary far-field patterns, Opt. Lett. **40**, 352 (2015).

[51] M. W. Hyde IV, Stochastic complex transmittance screens for synthesizing general partially coherent sources, J. Opt. Soc. Am. A **37**, 257 (2020).

[52] R. Tong, Z. Dong, Y. Chen, F. Wang, Y. Cai, and T. Setälä, Fast calculation of tightly focused random electromagnetic beams: Controlling the focal field by spatial coherence, Opt. Express **28**, 9713 (2020).

[53] Y. Chen, F. Wang, Z. Dong, Y. Cai, A. Norrman, J. J. Gil, A. T. Friberg, and T. Setälä, Polarimetric dimension and nonregularity of tightly focused light beams, Phys. Rev. A **101**, 053825 (2020).

[54] F. Wang, H. Lv, Y. Chen, Y. Cai, and O. Korotkova, Three modal decompositions of Gaussian Schell-model sources: Comparative analysis, Opt. Express **29**, 29676 (2021).

[55] H. Partanen, J. Turunen, and J. Tervo, Coherence measurement with digital micromirror device, Opt. Lett. **39**, 1034 (2014).

[56] K. Saastamoinen, L.-P. Leppänen, I. Vartiainen, A. T. Friberg, and T. Setälä, Spatial coherence of light measured by nanoscattering, Optica **5**, 67 (2018).

[57] Z. Huang, Y. Chen, F. Wang, S. A. Ponomarenko, and Y. Cai, Measuring Complex Degree of Coherence of Random Light Fields with Generalized Hanbury Brown–Twiss Experiment, Phys. Rev. Appl. **13**, 044042 (2020).

[58] Z. Dong, Z. Huang, Y. Chen, F. Wang, and Y. Cai, Measuring complex correlation matrix of partially coherent vector light via a generalized Hanbury Brown–Twiss experiment, Opt. Express **28**, 20634 (2020).

[59] J. R. Fienup, Reconstruction of an object from the modulus of its Fourier transform, Opt. Lett. **3**, 27 (1978).

[60] J. R. Fienup, Phase retrieval algorithms: A comparison, Appl. Opt. **21**, 2758 (1982).

[61] J. Bertolotti, E. G. van Putten, C. Blum, A. Lagendijk, W. L. Vos, and A. P. Mosk, Non-invasive imaging through opaque scattering layers, Nature **491**, 232 (2012).

[62] O. Katz, P. Heidmann, M. Fink, and S. Gigan, Non-invasive single-shot imaging through scattering layers and around corners via speckle correlations, Nat. Photonics. **8**, 784 (2014).

[63] D. Shen and D. Zhao, Measuring the topological charge of optical vortices with a twisting phase, Opt. Lett. **44**, 2334 (2019).

[64] J. W. Goodman, *Statistical Optics* (John Wiley & Sons, New York, 1985).

[65] H. Ni, C. Liang, F. Wang, Y. Chen, S. A. Ponomarenko, and Y. Cai, Non-Gaussian statistics of partially coherent light in atmospheric turbulence, Chin. Phys. B **29**, 064203 (2020).

[66] X. Zhu, J. Yu, Y. Chen, F Wang, O. Korotkova, and Y. Cai, Experimental synthesis of random light sources with circular coherence by digital micro-mirror device, Appl. Phys. Lett. **117**, 121102 (2020).

[67] X. Zhu, J. Yu, F. Wang, Y. Chen, Y. Cai, and O. Korotkova, Synthesis of vector nonuniformly correlated light beams by a single digital mirror device, Opt. Lett. **46**, 2996 (2021).